Geophysical Journal International

Geophys. J. Int. (2024) **237,** 203–216
Advance Access publication 2024 January 24
GJI Gravity, Geodesy and Tides

https://doi.org/10.1093/gji/ggae034

Mechanism and implications of the post-seismic deformation following the 2021 M_w 7.4 Maduo (Tibet) earthquake

Fei Chen [1], Faqi Diao [1], Mahmud Haghshenas Haghighi [2], Yuebing Wang,[3] Yage Zhu,[1] Rongjiang Wang[1] and Xiong Xiong [1]

[1] *Hubei Subsurface Multi-Scale Imaging Key Laboratory, School of Geophysics and Geomatics, China University of Geosciences, Wuhan* 430074*, China. E-mail: fqdiao@cug.edu.cn*
[2] *Institute of Photogrammetry and GeoInformation, Leibniz University Hannover, Hannover* 30167*, Germany*
[3] *China Earthquake Networks Center, Beijing* 100032*, China*

Accepted 2024 January 23. Received 2023 October 23; in original form 2023 July 17

SUMMARY

A major earthquake shook the Chinese county of Maduo, located in the Songpan-Ganzi terrane on the Tibetan Plateau, on 21 May 2021. Here, we investigate the post-seismic deformation process of this event, with the aim to understand the fault geometry, friction behaviour and regional rheology. To keep the self-consistency between co- and post-seismic deformation models, we first constrain the fault geometry and coseismic slip model of this event, which are directly used in modelling the post-seismic deformation. The coseimsic slip model reveals that the majority of coseismic slip is confined at the middle (3–15 km) of the brittle layer, leading to significant shallow slip deficit. Secondly, we obtain the post-seismic deformation in the first 450 d following the 2021 Maduo earthquake using the GPS and InSAR displacement time-series data. Thirdly, a combined model incorporating afterslip and viscoelastic relaxation is built to explain the observed post-seismic deformation. Our results suggest that the viscoelastic relaxation effect should be considered in the observation period, in order to avoid the unphysical deep afterslip in the ductile lower crustal layer. Combined analysis on viscosities inferred from this study and previous studies suggests a weak lower crust with steady-state viscosity of 10^{18}–10^{19} Pa s beneath the Songpan-Ganzi terrane, which may give rise to the distributed shear deformation and the development of subparallel secondary faults within the terrane. Besides, the inferred afterslip on uppermost patches of the middle fault segment suggests a rate-strengthening frictional behaviour that may be related to the coseismic slip deficit and rupture arrest of the Maduo earthquake.

Key words: Satellite geodesy; Numerical modelling; Time-series analysis; Rheology and friction of fault zones.

1 INTRODUCTION

The Songpan-Ganzi terrane (SGT) in the northeastern Tibetan Plateau plays an important role on the plateau's eastward extrusion and dynamic evolution (e.g. Tapponnier *et al.* 2001). The SGT accommodates significant sinistral motion by distributed interior shear deformation and development of several subparallel secondary faults (Wang & Shen 2020; Yue *et al.* 2022). In contrast, negligible interior deformation and few subparallel secondary faults are observed in the Qaidam basin and Qilian mountains to the north of the terrane. The mechanism behind above differences is crucial to regional tectonic deformation, but remains poorly understood. Meanwhile, several strong earthquakes ($M_w > 7$), including the 2021 M_w 7.4 Maduo earthquake, have occurred on the margin or within the SGT in the past two decades, defining it to be the most seismically active region in China (Yue *et al.* 2022).

The lower crustal rheology controls the strength of the crust, and thus plays an important role on regional tectonic deformation (Bürgmann & Dresen 2008). The post-seismic deformation recorded by geodetic observations is partially due to the viscoelastic relaxation of the deep ductile layer under the perturbations of the coseismic stress, and has been used to constrain the rheological properties and behaviours in areas surrounding the SGT (Liu *et al.* 2019; Zhao *et al.* 2021a; Chen *et al.* 2022). However, the rheological structure within the SGT was poorly studied due to the absence of large internal earthquakes. The Maduo earthquake, as an event within the SGT (Fig. 1), provides a unique opportunity to explore the interior rheological properties, which will further enrich

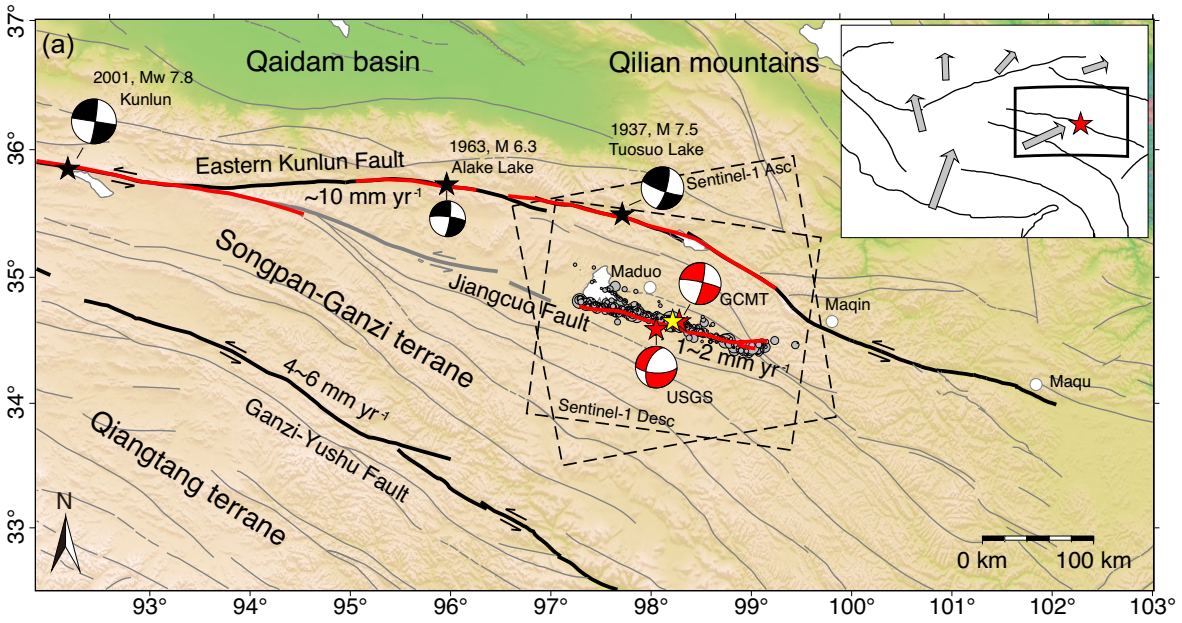

Figure 1. Tectonic setting of the 2021 M_w 7.4 Maduo earthquake. Solid black and grey lines denote the eastern Kunlun fault, the Ganzi-Yushu fault and secondary faults in the region. Red lines show the surface rupture trace of the M_w 7.4 Maduo earthquake (Pan *et al.* 2022) and three historical earthquakes (Diao *et al.* 2019). Grey dots show the surface projection of distribution of aftershocks till 30 May 2021 (Wang *et al.* 2021). Red beach balls and stars represent the focal mechanism and epicentre from Global Centroid-Moment-Tensor Project (GCMT) and United States Geological Survey (USGS). Dashed rectangles show the spatial extent of ascending and descending tracks of Sentinel-1 SAR data. The yellow star is the relocated epicentre (Wang *et al.* 2021). The interseismic slip rates of the Eastern Kunlun, Jiangcuo and Ganzi-Yushu faults are referred to S. Liu *et al.* (2019), Zhu *et al.* (2021) and Qiao *et al.* (2022).

the understanding of the rheological behaviour across the northeastern Tibetan Plateau. Several studies (He *et al.* 2021b; Fang *et al.* 2022; Xiong *et al.* 2022; Jin *et al.* 2023; Zhao *et al.* 2023) analysed the short-period post-seismic deformation (several months ~1 yr) following the event. Most of these studies suggested that afterslip is the dominant mechanism (He *et al.* 2021b; Fang *et al.* 2022; Xiong *et al.* 2022; Zhao *et al.* 2023), though significant deep afterslip is found in the ductile lower crust. Recently, Jin *et al.* (2023) suggested that a combined mechanism of afterslip and viscoelastic relaxation should be considered when modelling the post-seismic InSAR and GPS deformation in the first year after the event. Considering the complexity of the post-seismic deformation process, analysis with observations in longer periods may be required to constrain the model parameters involved in the modelling, and in-depth implications of the results on regional tectonic deformation should be carried out.

Besides, the slip behaviours of secondary faults within the SGT has not been well investigated due to absence of modern geophysical observations. After the Maduo event, both geophysical observations and field surveys were extensively collected to document the coseismic rupture characteristics and related slip behaviour of the Jiangcuo fault (Wang *et al.* 2021, 2022; Pan *et al.* 2022; Yuan *et al.* 2022). The previous studies revealed a bilateral asymmetric rupture process of the earthquake, that is, the rupture east of the hypocentre is larger and faster than that to the west, and the middle segment near the hypocentre may act as a barrier resisting the rupture propagation (He *et al.* 2021a; Li *et al.* 2022). Additionally, field investigations also suggested a large surface rupture gap in the middle barrier (longitude 98.2–98.5°; Yuan *et al.* 2022), which may reflect the variation of the frictional properties on the rupture fault. Further studies with combined analysis of coseismic rupture and aseismic afterslip can provide more constraints on the kinematic fault behaviour and associated frictional properties (Liu & Xu 2019).

In this study, we first invert for the fault geometry and coseismic slip distribution of the Maduo earthquake, which is the basis for the post-seismic deformation study. Next, we obtain the post-seismic deformation in the first 450 d following the Maduo earthquake using the GPS and InSAR displacement time-series. Then, we construct a combined model that incorporates the viscoelastic relaxation and aseismic afterslip to explain the observed post-seismic deformation. The modelling results can shed light on the lower crustal rheology within the SGT and the distribution of afterslip on the Jiangcuo fault. Finally, we discuss the reliability of our inferred results and their implications on regional tectonic deformation and fault frictional properties.

2 GEODETIC OBSERVATIONS

2.1 Processing of the InSAR data

Here we use differential InSAR and sub-Pixel Offset Tracking (sPOT) to obtain the line-of-sight (LOS) displacements and the range displacements along the satellite azimuth and range direction of the coseismic signal, respectively. We use the data from the Sentinel-1 catalogue of the Copernicus Programme satellite constellation operated by the European Space Agency (ESA), covering the earthquake episodes in both ascending and descending orbits. We collect the post-seismic SAR data only 4 d after the event, suggesting that the obtained deformation is dominated mainly by coseismic rupture. And we obtain four geodetic datasets with different geometric viewing parameters, that is displacements in the LOS and range directions (Fig. 2).

We process the Sentinel-1 SAR data using the GAMMA software (Wegnüller *et al.* 2016). Table S1 summarizes the details of SAR data used in this study. Along each track of the Sentinel-1 satellite, we stitch SAR frames to cover the large earthquake seismic area, and update the orbital data of SAR images using POD Restituted Orbit

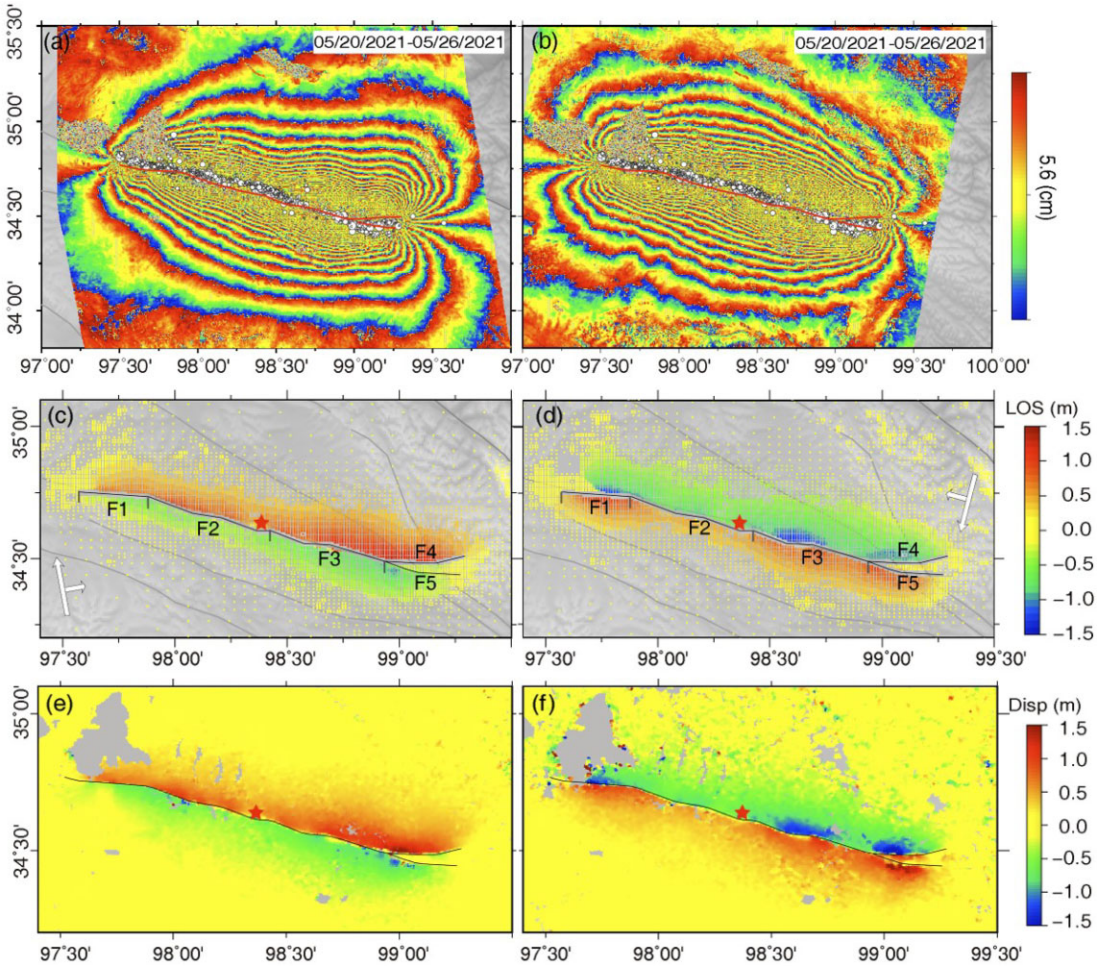

Figure 2. Panels (a) and (b) show Sentinel-1 InSAR interferograms from ascending and descending tracks, respectively. Panels (c) and (d) show unwrapped displacements in the line of sight directions. Panels (e) and (f) draw displacements in range directions based on the sub-Pixel Offset Tracking (sPOT) processing. Red star shows the relocated earthquake epicentre (Wang *et al.* 2021). White dots represent aftershocks provided by Wang *et al.* (2021) as shown in Fig. 1. Red and black lines show the surface rupture trace (Pan *et al.* 2022). F1–F5 in (c) and (d) denote five fault segments.

data obtained from Alaska Satellite Facility (ASF). After a precise TOPS coregistration of images, we calculate the interferometric phase. Then, we multilook interferograms by a factor of 10 in range and 2 in azimuth leading to approximately 25 m × 25 m ground pixel size. We reduce the topographic phase component from the interferogram using a 3 arcsec SRTM DEM (Farr & Kobrick 2000). Then we filter the interferometric phase using an adaptive filter with an exponent of 0.4 and a window size of 32 in range and azimuth to enhance the phase quality (Baran *et al.* 2003). Next, we perform phase unwrapping using the minimum cost flow algorithm (Chen & Zebker 2001) and convert unwrapped phase information to the metric displacement measures. Before using the results in the modelling, we downsample the displacement maps using a quadtree method to reduce the density of pixels in areas with low gradient of displacement (Simons *et al.* 2002).

For each track of Sentinel-1 data, we also apply offset tracking analysis (Michel *et al.* 1999). Using the precise coregistration information of pre- and post-seismic images, we convert range and azimuth offsets to displacements in the corresponding directions. We use a cross-correlation window of 100 in range and 20 in azimuth. We also filter the offset tracking results using a median filter with a 15 × 15 kernel size in order to increase the signal-to-noise ratio.

To measure the post-seismic deformation signal from each track of Sentinel-1 data (details shown in Table S2), we apply a small baseline analysis (Berardino *et al.* 2002) to all interferograms generated in GAMMA. In each ascending and descending track, first, we coregister SAR images and InSAR maps to a common reference image. Then, we connect each resampled image to its next three consecutive images to form a small baseline network (Fig. S1). The small baseline interferograms are then generated, multilooked, and unwrapped similar to the processing of coseismic interferograms.

We use the small baseline implementation in MintPy (Zhang *et al.* 2019) to perform time-series analysis of the stack of interferograms. Then, we adopt a coherence threshold of 0.4 to mask out noisy pixels and keep reliable pixels in the time-series analysis. After inversion of the interferogram network and estimation of the time-series, we correct the tropospheric phase delay using PyAPS (e.g. Jolivet *et al.* 2011) and ECMWF ERA5 data (Muñoz-Sabater 2019). Furthermore, we estimate and remove the residual DEM error (Fattahi & Amelung 2013). In addition, we subtract a linear ramp from the unwrapped interferograms to account for remaining long-wavelength errors. To estimate the correction ramp, we mask out the near-fault deformation area.

When investigating the post-seismic deformation field, other non-post-seismic signals have to be eliminated. The permafrost effect on ground vertical deformation may be expected as shown by previous studies due to the thawing and freezing of the ice in the active layer (e.g. Chen *et al.* 2022). Meanwhile, the deformation amplitude of the permafrost effect can reach up to 4 cm, and varies spatially with local geological conditions estimated by Chen *et al.* (2022). The original observed InSAR displacement time-series exhibits a seasonal (yearly) deformation (Fig. S2), similar to that of the permafrost effect (Chen *et al.* 2022). The seasonal deformation in seismic source area may be dominated by the permafrost effect. Therefore, we use an annual oscillation function to model the effect, and fix the phase deviation based on the finding reported by Chen *et al.* (2022). We isolate the pure post-seismic displacement time-series using a logarithmic function (e.g. Freed *et al.* 2017; Hong & Liu 2021; Nikolaidis 2002). Therefore, we fit the original displacement time-series on each pixel based on eq. (1) (Figs 3 and S2). We note an asymmetric InSAR displacement in far-field areas, especially for that of the descending track, as observed by Jin *et al.* (2023). This may be induced by the lateral variation of viscosity across the fault, however we cannot exclude other possibilities, such as the observation noises (e.g. imprecise atmospheric correction).

$$D_{los} = a_1 + a_2 \ln(1 + t/\tau) + a_3 \cos(2\pi t + a_4), \quad (1)$$

where D_{los} is the observed LOS displacement time-series, $a_1 \ldots a_4$ and τ are unknown coefficients need to be solved. a_1 is a static offset, and a_2, a_3 represent the amplitude of the post-seismic deformation and the seasonal deformation, respectively. a_4 is the phase deviation with the range of $\pi/6 \sim \pi/2$ based on the result of Chen *et al.* (2022). t is the time (year) after the Maduo earthquake, and τ is the character decay time.

2.2 Processing of the GPS data

Besides the post-seismic InSAR data, we also use the GPS data to measure the post-seismic deformation following the 2021 M_w 7.4 Maduo earthquake. Within a radius of about 200 km around the epicentre, a total of 4 continuous and 21 campaign GPS stations had been established ~15 yr prior to the Maduo earthquake. These stations recorded both the pre- and post-seismic deformation of the event. We process the daily raw GPS data using the strategy proposed by Gan *et al.* (2007). To process the daily raw GPS data, we first use the GAMIT software (Herring *et al.* 2010a) to get the loosely constrained daily solutions. Then, we adopt the GLOBK software (Herring *et al.* 2010b) to combine the loosely constrained daily solutions and global solutions obtained from the Scripps Orbital and Position Analysis Centre (http://sopac.ucsd.edu). Finally, we fix the combined solutions to the ITRF08 reference frame with constraint from 80 tracking stations preserved by the International GNSS Service. After obtained the raw GPS displacement time-series, we adopt the following equations to fitting the GPS continuous and campaign solutions. We assume that the post-seismic deformation follows a logarithmic decay trend, which is suitable for both continuous observation and campaign observation with three post-seismic epochs (e.g. Nikolaidis 2002; Freed *et al.* 2017; Hong & Liu 2021; Fig. S3). However, for some campaign GPS data with a limited number of post-seismic epochs (only two), the logarithmic decay trend cannot be constrained. Therefore, we adopt a linear fitted approach for these data.

$$\begin{aligned} F_{Obs_{cont}} &= a_1 + a_2 t + H(t - t_0) a_3 + H(t - t_0) a_4 \ln(1 + (t)/a_5) \\ &\quad + a_6 \cos(2\pi t) + a_7 \sin(2\pi t) + a_8 \cos(4\pi t) + a_9 \sin(4\pi t) \end{aligned} \quad (2)$$

$$F_{Obs\_camp2} = a_1 + a_2 t + H(t - t_0) a_3 + H(t - t_0) a_4 t \quad (3)$$

$$F_{Obs\_camp3} = a_1 + a_2 t + H(t - t_0) a_3 + H(t - t_0) a_4 \ln(1 + (t)/a_5), \quad (4)$$

where F_{Obs_cont}, F_{Obs_camp2}, F_{Obs_camp3} represent the fitted GPS displacement time-series of the continuous stations, campaign stations with two and three post-seismic epochs, respectively. a_1-a_9 are the unknown coefficients to be solved. The first four items in these equations are static offset, long-term deformation rate, co- and post-seismic deformation, respectively. The last four terms in eq. (2) represent the annual and semi-annual components of the seasonal deformation. $H(t - t_0)$ represents the Heaviside function, where t and t_0 are the time of the displacement time-series and the event.

After the above data processing, we obtain the post-seismic GPS and InSAR displacement time-series in the first 450 d after the earthquake (Figs S2 and S3). We show the accumulated displacements in this time period in Figs 3(a) and (b). We observe a maximum GPS displacement of ~40 mm on the QHMD station, ~25 km from the fault (Fig. 3). Additionally, we find clear GPS displacements of ~5 mm in areas >100 km from the fault. The inferred InSAR displacements indicate significant near-field deformation across the fault. In addition, we find a general consistency between GPS and InSAR displacements (Figs 3c–f), suggesting the reliability of the post-seismic deformations that inferred from different techniques.

3 COSEISMIC DEFORMATION MODELLING

3.1 Modelling and fault geometry

The coseismic slip model is the basis of the post-seismic deformation modelling, as it provides the fault geometry of the afterslip model and serve as the driving source of the viscoelastic relaxation model (e.g. Freed *et al.* 2017). Meanwhile, it is important to maintain the self-consistency (e.g. fault geometry and methodology) between the co- and post-seismic deformation models (Freed *et al.* 2017). Thus, we first use the coseismic InSAR data (Fig. 2) to invert for coseismic slip distribution, instead of using one from a separated study.

We use finite-fault source modelling to probe the fault geometry and slip distribution of the Maduo earthquake that can well fit the coseismic InSAR observations. For this aim, we utilize a constrained least squares method (Wang *et al.* 2013), which can build complex fault geometry with simple parameter configuration. To make the solution stable, we add an *a-priori* smoothing constraint in the cost function:

$$F(s) = \|Gs - y\|^2 + \alpha^2 \|Hs\|^2, \quad (5)$$

where s is the slip vector of each fault patch; G is the Green's function matrix calculated by the crustal elastic parameters (e.g. seismic velocity, density) from Wang *et al.* (2021) in the region of the Maduo earthquake; y is the observation data, including InSAR LOS and sPOT range displacements; H represents the finite difference approximation of the Laplacian operator; α is the smoothing factor, which controls the trade-off between the model roughness and misfit.

We divide the fault plane into five segments (F1–F5) to match the detailed surface rupture trace (Pan *et al.* 2022; Yuan *et al.*

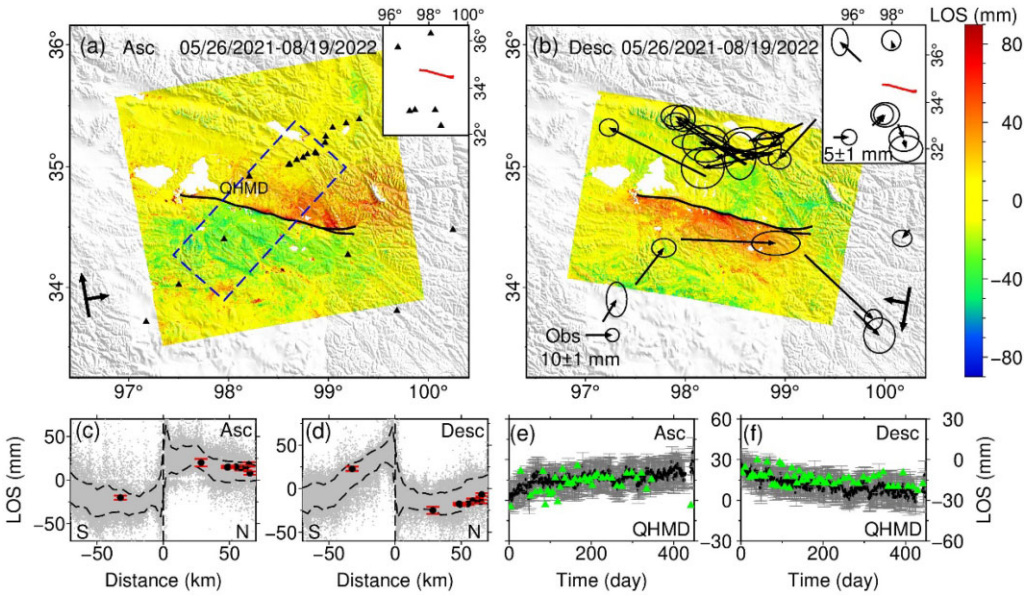

Figure 3. Panels (a) and (b) show accumulated post-seismic GPS and InSAR LOS displacements in the first 450 d after the event from ascending and descending tracks, respectively. Positive values are moving close to the satellite. Black triangles are locations of GPS stations. Subgraphs show the GPS data in the far-field areas. Panels (c) and (d) show the comparison between the GPS (black dots) and InSAR (grey dots) data (in LOS directions) within dashed rectangle in (a). Horizontal axis denotes the distance along the swath. Dashed curves in (c) and (d) show the 1σ uncertainties of InSAR data. Panels (e) and (f) show the comparison between the InSAR (green triangles) and GPS (black dots) time-series at the QHMD station in the LOS directions.

2022) and the local alignment of aftershocks (Fig. 2a). A fault with spatial scales of 160 km along strike and 27 km along dip is built, which is then subdivided into patches with a constant size of 3 × 3 km^2 to solve for the slip distribution. We find the optimal dip angle of each fault segment with a grid-search method when probing the coseismic slip distribution (Feng *et al.* 2020; Zhang *et al.* 2021). As shown in Figs 4(a) and S4, the optimal dip angles are 80° and 65° to the north for the segments F1 and F2, respectively, and are 90° for segments F3 and F4. The dip angle of the eastern branch F5 is also set to 90°, which is similar to previous inversion studies (He *et al.* 2021b; Li *et al.* 2022). We vary the dip angle smoothly at the connection of adjacent fault segments to avoid sudden fault geometry changes. We obtain the weighting of the smoothing constraint (0.02) based on the trade-off curve between model roughness and data misfit (Fig. 4b).

3.2 The coseismic rupture model

As shown in Fig. 4(a), the best-fitting slip distribution of the Maduo earthquake reveals that this event ruptured the Jiangcuo fault along strike by up to 160 km, showing a clear asymmetrical rupture character as that shown in previous studies (Jin & Fialko 2021; He *et al.* 2021a, b; Zhao *et al.* 2021b; Li *et al.* 2022; Yue *et al.* 2022). Fault slip below two surface rupture gaps (read lines in Fig. 4a) is relatively small, which agrees with field investigation (Yuan *et al.* 2022). We find that most coseismic slip occurs at the middle (3–15 km) of the brittle layer and slip to the west of the hypocentre is lower than that to the east of the hypocentre (Fig. 4a), leading to the clear shallow slip deficit, as shown in other earthquakes (Fig. 4c). We will discuss fault frictional behaviour revealed by the coseismic shallow slip deficit in Section 5.4. Our coseismic slip model suggests a geodetic moment of ∼1.76 × 10^{20} N m (M_w 7.43).

The optimal coseismic slip model can explain the observed InSAR and sPOT data reasonably well, although we observe some local residuals near the fault trace (Fig. 5). We interpret local near-fault residuals mainly relate to inelastic deformation, heterogeneous materials or a more complex geometry of the faults that are not considered in our model or the unwrapping error due to large phase gradient across the rupture. We perform checkerboard tests to investigate the resolving power of data, and find that the input slip asperities of 24 km × 12 km or 12 km × 12 km (length × width) can be recovered well in terms of location and slip magnitude (Fig. S5). We also perform synthetic tests to identify the reliability of the obtained fault dip angles. The input dip angle of each segment can be identified (Fig. S4), suggesting that the geodetic observations can provide constraint on fault geometric parameters.

4 POST-SEISMIC DEFORMATION MODELLING

4.1 Construction of the combined model incorporating afterslip and viscoelastic relaxation

Aseismic afterslip and viscoelastic relaxation of the lower crust/upper mantle are proposed as the two main mechanisms responsible for post-seismic deformations following large earthquakes (Bürgmann & Dresen 2008; Wang *et al.* 2012; Freed *et al.* 2017). Besides, the poroelastic rebound can also produce post-seismic deformation with low magnitude near the rupture faults (Jónsson *et al.* 2003), which has been generally ignored due to a lack of effective observations. Moreover, afterslip is assumed as the dominant mechanism for post-seismic deformations at initial stages, however, recent studies revealed that the viscoelastic relaxation should be considered even in early post-seismic periods (e.g. Sun *et al.* 2014; Diao *et al.* 2021; Fukuda & Johnson 2021). Therefore, we construct a combined model of viscoelastic relaxation and afterslip directly, rather than testing the performance of a separated mechanism at first. We discuss the limitation of separated mechanisms (afterslip, viscoelastic relaxation and poroelastic rebound) in Section 5.2.

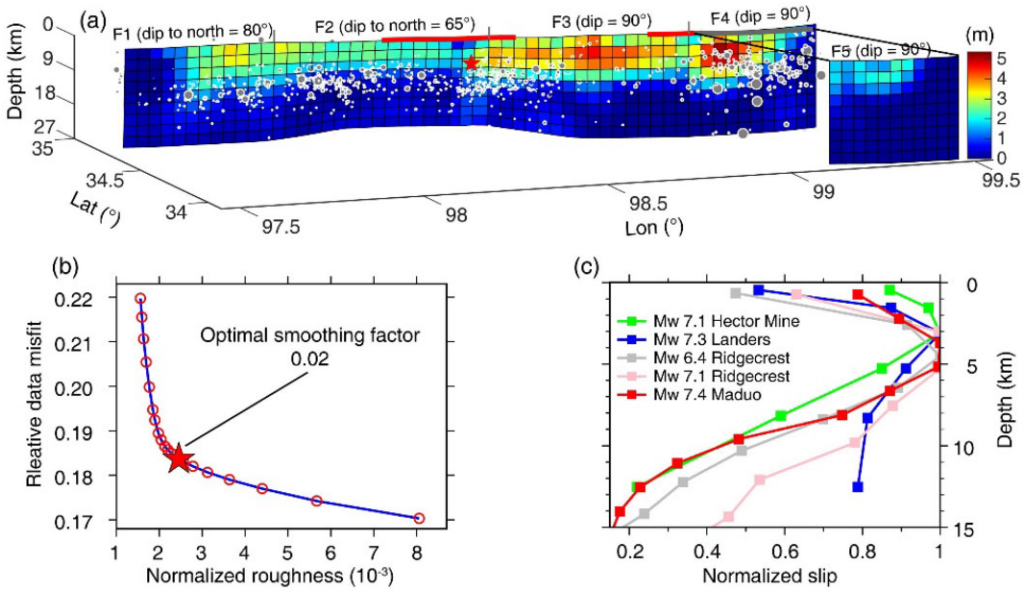

Figure 4. Results of coseismic slip model. (a) Coseismic slip model of Maduo earthquake. Grey dots are aftershocks, as depicted in Fig. 1. Red star and lines denote the hypocentre and rupture gaps shown in Yuan *et al.* (2022), respectively. (b) Trade-off curve between normalized roughness and relative data misfit used for determining the smoothing factor for the inversion. (c) Variation of along-strike averaged normalized coseismic slip of the event with depth, as well as for other strike-slip earthquakes inferred from C. Liu *et al.* (2019).

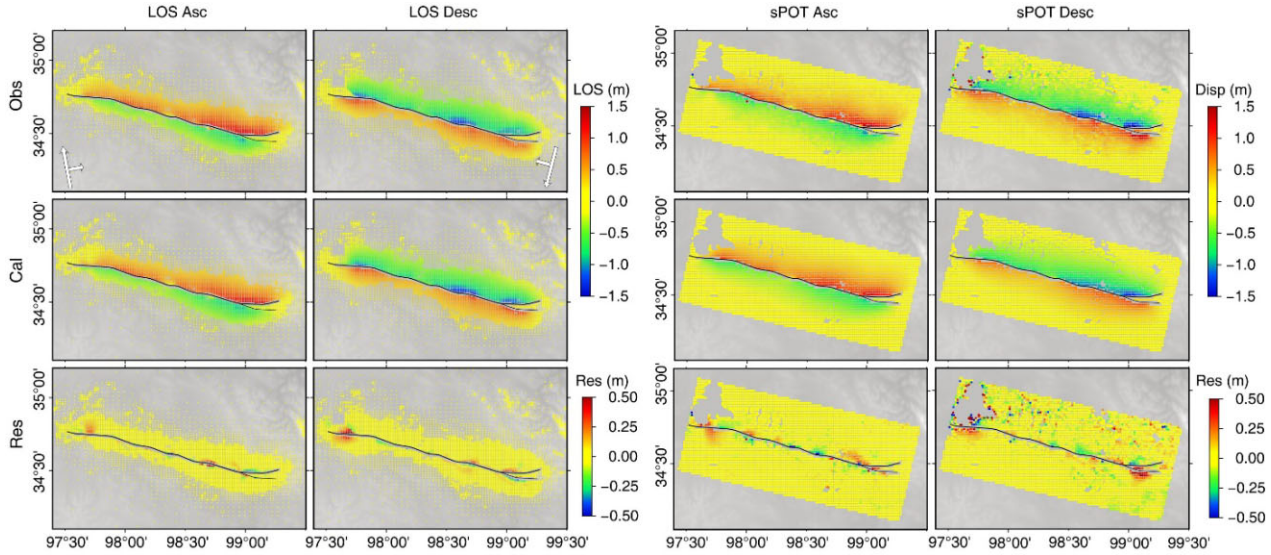

Figure 5. The comparison of the observed and modelled coseismic displacements in LOS (two columns on the left) and range directions (two columns on the right) of ascending and descending tracks.

The procedure for constructing the combined post-seismic deformation model is as follows. First, we assume that the post-seismic deformation on far-field GPS stations (>45 km from the fault) is governed by the viscoelastic relaxation effect of the lower crust, and estimate the optimal lower crustal rheological parameters in the viscoelastic relaxation model based on these GPS data. Then, we remove the viscoelastic relaxation effect in the InSAR displacement time-series and use the residual to invert for the time-dependent fault afterslip. Thirdly, we estimate the far-field effect due to obtained afterslip and remove it from the GPS observation. Finally, we repeat the aforementioned steps until the solution converges. For the afterslip inversions, we utilize the same approach as that used for the coseismic slip inversion in Section 3.1. We maintain the consistency of the fault geometry between the coseismic slip model and the afterslip model, but extend the fault width along the downdip direction to 60 km, which is deep enough to include the deep afterslip. We also use the 'trade-off' method same as that in the coseismic slip inversions to obtain the optimal smoothing factor.

We simulate the viscoelastic relaxation effect of the Maduo earthquake based on a layered viscoelastic half-space model using the PSGRN/PSCMP code developed by Wang *et al.* (2006). In our model, we set the thicknesses of the upper crust and lower crust to 20 and 40 km, respectively, following Diao *et al.* (2019) and Xiong *et al.* (2010). The elastic parameters (e.g. seismic velocity, density) are inferred from the seismic inversion result of Wang *et al.* (2021). We adopt the Burgers rheology body due to its ability to capture

the transient and steady-state deformation of the viscoelastic layers (Fukuda & Johnson 2021). The Burgers model we used contains three parameters: the transient viscosity η_k, steady-state viscosity η_m and the ratio between the effective and the unrelaxed shear modulus (α, i.e. $\mu_k/(\mu_k+\mu_m)$). We fix the ratio (η_k/η_m) at 0.1 based on many previous studies (e.g. Hu *et al.* 2016; Tian *et al.* 2020). For the upper mantle, we fix the steady-state viscosity at 1×10^{20} Pa s and test its influence in Section 5.1. Thus, there are only two free parameters in the lower crustal layer of the viscoelastic relaxation model, α and η_m^l (steady-sate viscosity of the lower crust). We use the grid search approach to optimize the viscosity parameters (Diao *et al.* 2021), and define the misfit function as follows:

$$F\left(\eta_m^l,\ \alpha\right) = \sum_{i=1}^{M} 1/M \sqrt{\sum_{j=1}^{N} \sigma_j^{-2} \left| U_{obs}^j - U_{cal}^j \right|^2 / N}, \quad (6)$$

where F is the root mean square (RMS) residual. U_{obs}^j and U_{cal}^j are the observed and simulated GPS displacement time-series in the viscoelastic relaxation model, respectively. σ is the observation error. i and j are the indexes of the GPS station and time samples of displacement time-series on the station. N is the number of the time samples on each GPS station, and M is the number of GPS stations.

4.2 Results of the combined model

As shown in Fig. 6(a), the inferred optimal values for η_m^l and α are 1×10^{19} Pa s and 0.7, respectively. The value of α had been assumed to be 0.5 in previous studies (Hu *et al.* 2016), however, we find that this assumption fails to capture the temporal evolution of the GPS displacement time-series. The optimal afterslip distribution in the combined model is shown in Fig. 6(b). Notably, we observe significant shallow afterslip in the middle north-dipping segment (longitude 98.2–98.7°), where the coseismic slip is relatively low. Besides, there are some isolated afterslip on deep patches below the aftershock cloud, which is discussed in Section 5.2. The geodetic moment released by the afterslip is about 1.27×10^{19} N m, corresponding to an M_w 6.67 earthquake.

Our model can explain the cumulative GPS and InSAR displacements well in terms of deformation magnitude and pattern (Figs 7 and 8). The InSAR residuals approximately follow a normal distribution with a mean value near zero, indicating the absence of any systematic error. Furthermore, the combined model can generally capture the temporal evolution of the GPS and InSAR observations (Figs 7, 8 and Fig. S6), including the GPS data (e.g. the data on the QHMD station) that do not participate in the inversion.

5 DISCUSSION

5.1 Analysis on the reliability of the obtained results

Compared to the InSAR data used in previous studies (He *et al.* 2021b; Fang *et al.* 2022; Xiong *et al.* 2022; Zhao *et al.* 2023), we extend the time span of geodetic observations and remove the seasonal deformation (e.g. the permafrost effect), which can effectively suppress the noise and make the post-seismic deformation signal more reliable. Furthermore, compared to the GPS data shown in Xiong *et al.* (2022), the GPS observations we used are located in the mid to far-field, which will be less affected by afterslip, thus can better constrain the rheological structures and properties beneath the seismic source region. The inferred steady-state lower crustal viscosity (1×10^{19} Pa s) is similar to that of Jin *et al.* (2023), which also indicates the reliability of our results. The combined data from InSAR and GPS observations can provide stronger constraints for the post-seismic deformation process of the Maduo earthquake.

To reduce the number of free parameters, we fix the thickness of the lower crust and the viscosity of the upper mantle in the combined model. To discuss the effect of fixing these parameters, further tests are carried out. First, we consider three different lower crustal thicknesses: 30, 40 and 50 km, and search for the optimal viscosity using the approach described in Section 4.1. As shown in Fig. 9(a), the optimal viscosity varies slightly with different lower crust thicknesses (8×10^{18}–1×10^{19} Pa s). Therefore, we infer that a value of $\sim10^{19}$ Pa s is reasonable for the optimal lower crust viscosity. Secondly, we test different values for the steady-state viscosity of the upper mantle. The result suggests that RMS is minimum when the viscosity is located at 1×10^{20} Pa s (Fig. 9b). Therefore, it is reasonable to fix this parameter at 1×10^{20} Pa s. Finally, we assume the displacements on GPS stations >45 km from the fault are mainly driven by the viscoelastic relaxation effect. As shown in Fig. 8(b), the effect of afterslip on these GPS stations is negligible compared to that of the viscoelastic relaxation effect, supporting our assumption. As demonstrated in Section 4.1, we also use an iterative method to obtain the viscosity in the combined model, which will decrease the effect of afterslip on these far-field GPS stations.

5.2 Contribution of afterslip and viscoelastic relaxation to the observed post-seismic deformation

A displacement profile across the fault shows the separated contribution of afterslip and viscoelastic relaxation in the combined model (Figs 7i and j). It is clear that the afterslip governs the deformation near the fault and decays rapidly with distance from the fault. In contrast, the deformation caused by the viscoelastic relaxation effect is negligible in the near-field area, but it gradually increases and becomes dominant in areas >20 km from the fault. Our results highlight that afterslip and viscoelastic relaxation complement each other in controlling the post-seismic deformation. Similar findings have been obtained in studies of post-seismic deformation following the 2015 Nepal earthquake and the 2011 Tohoku earthquake (e.g. Sun *et al.* 2014; Diao *et al.* 2021). To demonstrate the limitation of the separated mechanisms, we explore their performance as follows.

We first assume that afterslip is the only mechanism responsible for the observed post-seismic GPS and InSAR deformation. Using the same inversion method and geodetic data, we get the distribution of the pure afterslip model (Fig. 10a). We find that widespread deep afterslip at depths below 30 km is required to explain the post-seismic deformation (Figs 10b–g). Compared with the afterslip obtained in the combined model, we infer that these deep afterslip are resulted from the overuse of this mechanism, which only reflect the depth of the driving source, where the viscoelastic relaxation may actually occur. Thus, the deep afterslip obtained based on the assumption of a pure afterslip mechanism are perhaps an illusion, which should be carefully discriminated. By including the viscoelastic relaxation, the deep afterslip in the pure afterslip model is decreased by 80 per cent, although slight deep afterslip still exists (Fig. 6b). These residual deep afterslip may be induced by the simplified viscoelastic relaxation model that neglects the lateral variation of the viscosity.

Then, we consider the pure viscoelastic relaxation separately. Constrained by the GPS and InSAR data, we search the optimal

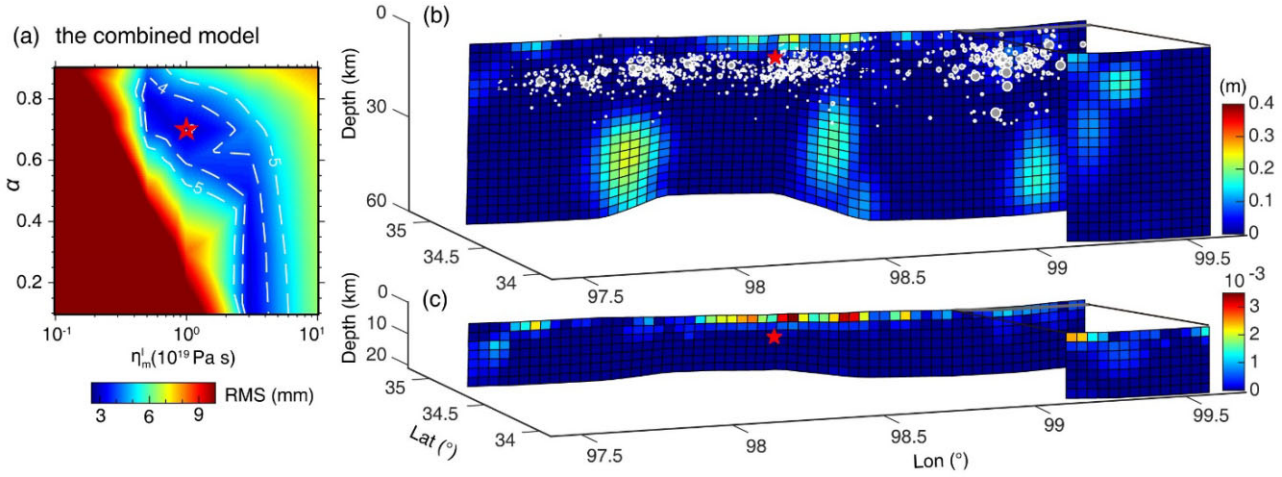

Figure 6. The results of the combined model. (a) The RMS residual varies with different combination (α, η_m^l) of viscoelastic relaxation model. Red star defines inferred optimal parameters. (b) The inferred optimal afterslip model in the combined model. Grey dots are aftershocks, as shown in Fig. 1. Red star denotes hypocentre. (c) Inferred frictional parameter $a - b$ values on the Jiangcuo fault.

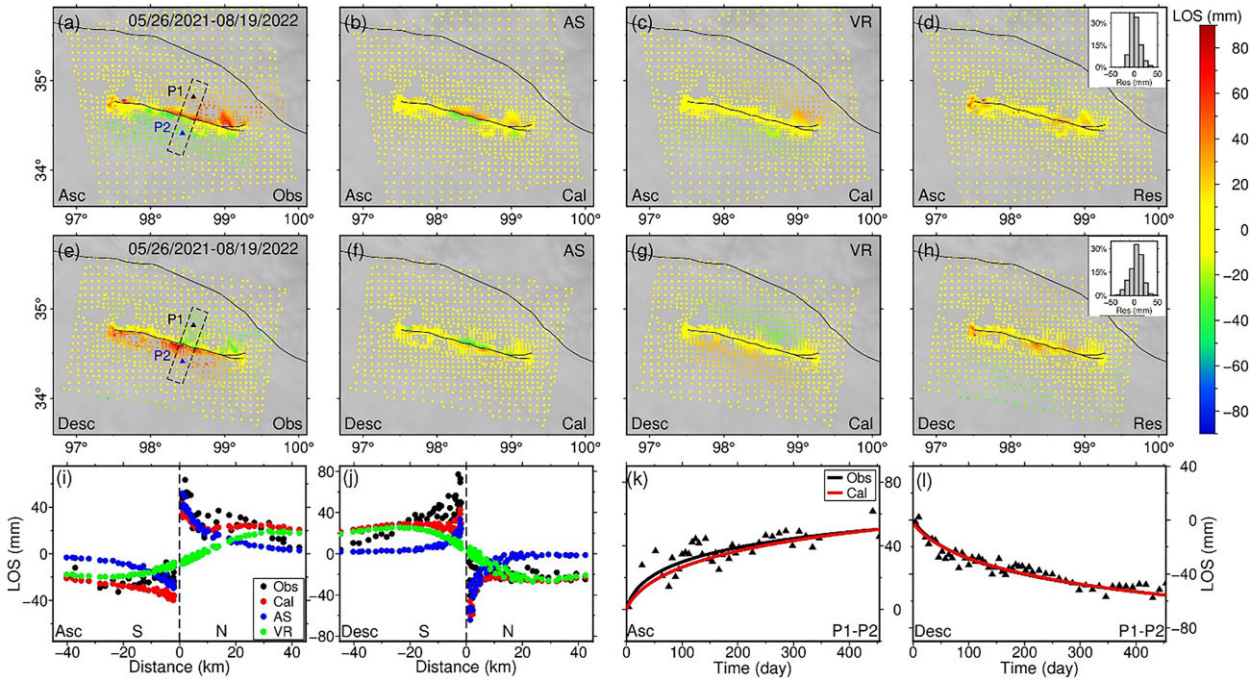

Figure 7. Comparisons between the observed and modelled post-seismic InSAR displacements. Panels (a)–(d) are observations, predictions and residuals for post-seismic LOS displacements for the ascending track, while panels (e)–(h) are those for the descending track. Panels (i) and (j) show detailed comparison of InSAR data on a profile perpendicular to the fault [dashed box in (a)]. AS and VR represent deformations caused by the afterslip and viscoelastic relaxation model. Panels (k) and (l) show comparisons between observations [deformation difference on two pixels (P1–P2)] and predictions. Black triangles are the observed displacement time-series.

parameters in the pure viscoelastic relaxation model using the same grid-search method presented in the combined model. As shown in Fig. 11, the inferred optimal model parameters are close to that obtained in the combined model, however, the yield model residual of ∼6 mm is two times larger than that of the combined model (∼3 mm). More importantly, although the pure viscoelastic relaxation model clearly can explain the far-field GPS displacements reasonably, it clearly fails to capture the near-field InSAR observations (Fig. 11), suggesting that the afterslip on shallow patches are necessary.

Finally, we evaluate the poroelastic rebound effect. Using a method shown in many previous studies (e.g. Diao *et al.* 2018), we first set different Poisson ratios, that is 0.25 and 0.21 for materials in the poroelastic layer (<4 km depth), to represent the undrained and drained conditions. Then, with these two scenarios we calculate the coseismic displacements on each InSAR point, and obtain the stable effect of the poroelastic rebound by differencing these two coseismic displacement fields. As shown in Fig. 12, the deformation caused by this mechanism is limited in near-field areas, which is hard to explain the observed post-seismic deformation (Figs 7a and e). The simulated deformation also fails to capture the residual

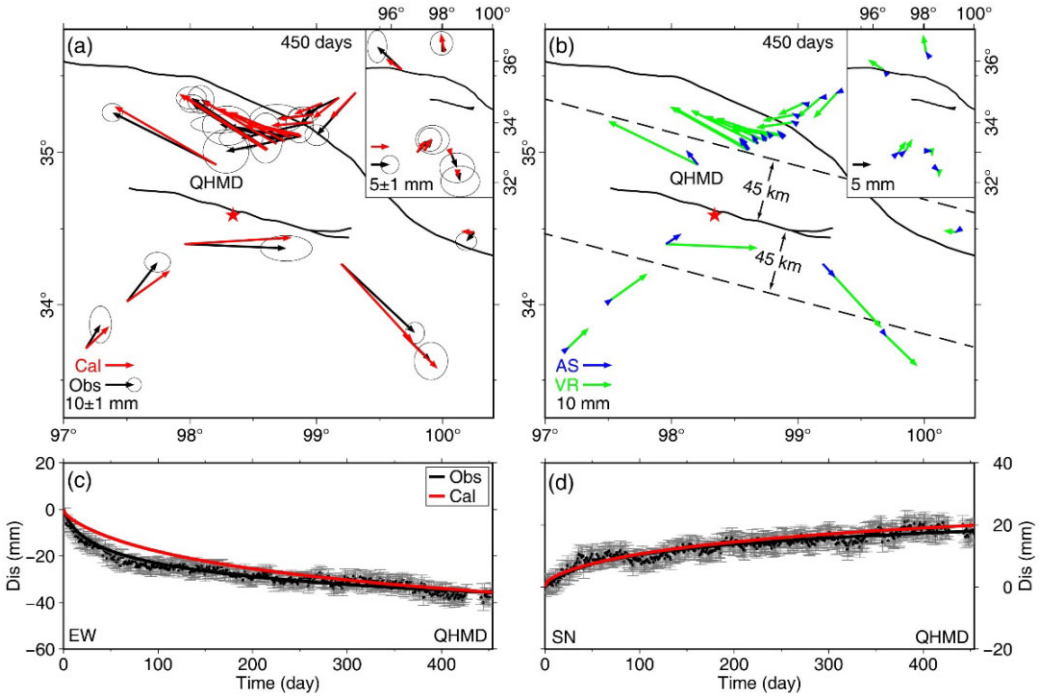

Figure 8. Comparisons between the observed and calculated post-seismic GPS displacements. Panel (a) shows the comparison between the cumulative GPS displacements (black vector) and predictions of the combined model (red vector). Panel (b) shows the contributions of the afterslip (blue vector) and viscoelastic relaxation (green vector) in the combined model. Panels (c) and (d) are comparisons between observed and predicted displacement time-series at the QHMD station.

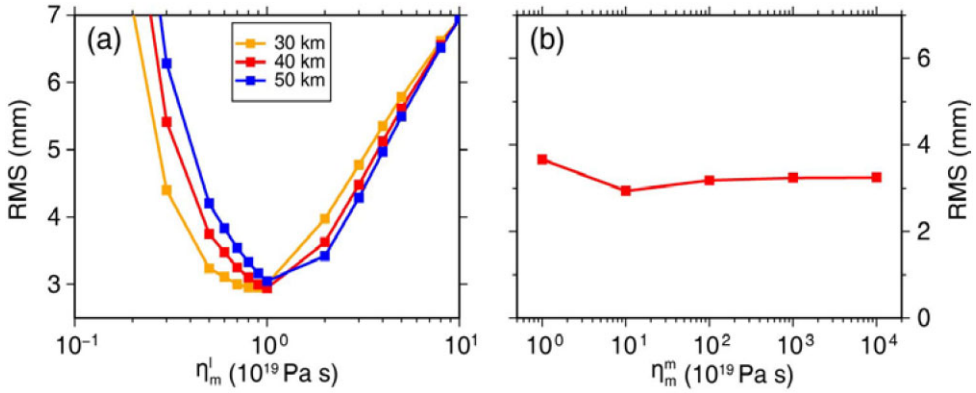

Figure 9. The effect of the lower crustal thickness and the steady-state viscosity of the upper mantle. (a) The RMS residual variation with η^l_m (steady-state viscosity of the lower crust) under different lower crustal thicknesses. (b) The RMS residual variation with different upper mantle viscosities (η^m_m).

displacements of the combined model (Figs 7d and h). Therefore, we ignore this effect in our combined model.

5.3 Implications on the inferred regional rheological structure

The rheological structure of the SGT has been investigated based on post-seismic deformation studies of historical major earthquakes (Liu *et al.* 2019; Zhao *et al.* 2021a; Chen *et al.* 2022). Combining our results with previous geodetic studies, we find that the lower crustal viscosity within the SGT is lower (10^{18}–10^{19} Pa s) than that of its northern neighbouring blocks, that is the Qaidam basin and Qilian Mountains. Furthermore, we find a gradual increase of lower crustal viscosity from south to north across northeastern Tibet (Fig. 13). Geophysical observations indicated zones of low *S*-wave velocity and high conductivity in the lower crust beneath the terrane (Jiang *et al.* 2014; Zhan *et al.* 2021), which is consistent with the inferred low viscosity in this study. All these geophysical investigations suggest a weak and ductile layer that may allow lower crustal flow as indicated in many previous studies (Clark & Royden 2000; Royden *et al.* 2008).

Both the geodetic observations (Li *et al.* 2023) and the field investigations (Yuan *et al.* 2022) indicate that the Maduo earthquake occurred on the Jiangcuo fault—a secondary fault within the SGT. Actually, besides the Jiangcuo fault, several subparallel secondary faults, such as the Dari fault and Wudaoliang-Changshagongma fault, had been developed in the terrane (Fig. 13). The development of these subparallel secondary faults shows a general consistence with the distributed interior shear deformation as inferred from

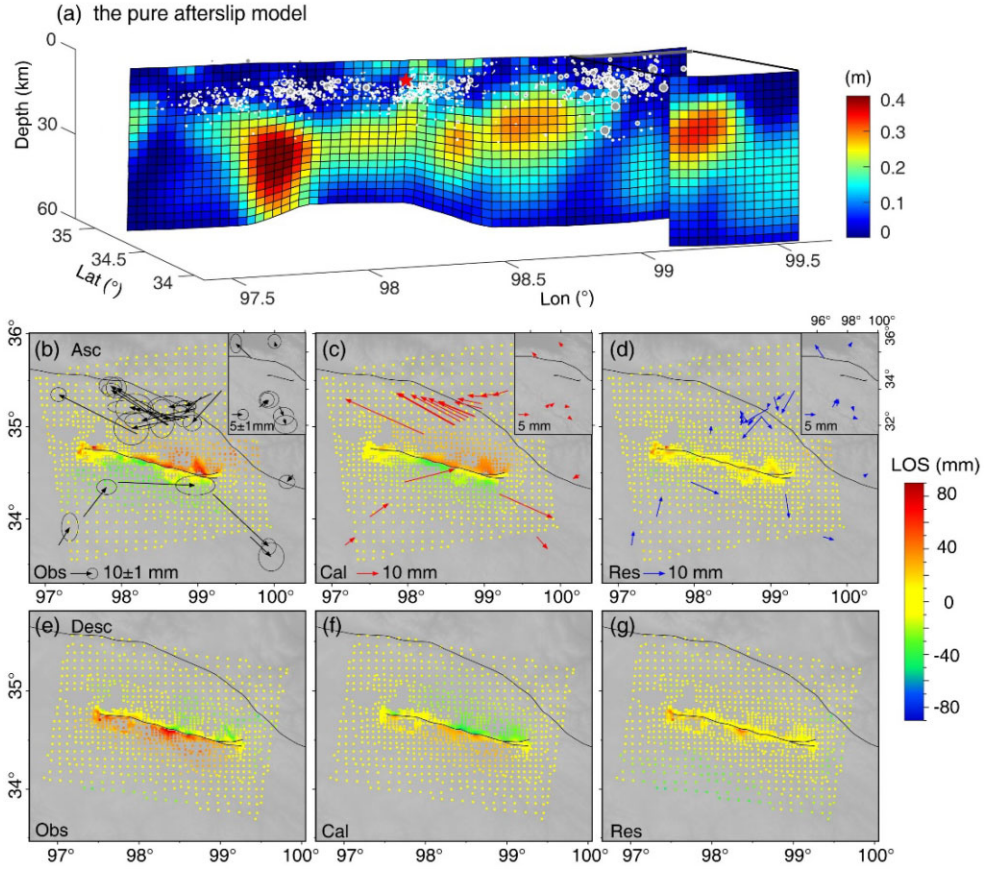

Figure 10. The inversion result and data-fitting of the pure afterslip model. Panel (a) shows the inverted pure afterslip model. Panels (b)–(d) show the observation, prediction, and residual of post-seismic LOS displacements of ascending track and those for post-seismic GPS displacements, while panels (e)–(g) are those for the descending track.

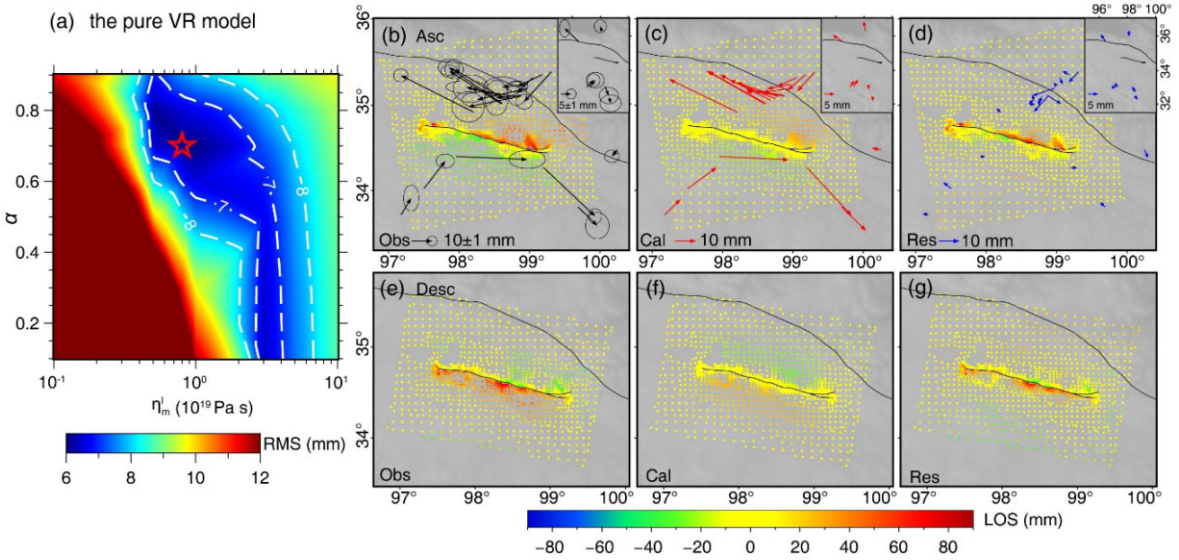

Figure 11. The searching result and data-fitting of the pure viscoelastic relaxation (VR) model. Panel (a) shows the RMS residual varies with different combination of (α, η^l_m). The red star defines the optimal viscosity parameters. Panels (b)–(d) are observation, prediction and residual for post-seismic LOS displacements of ascending track and those for post-seismic GPS displacements, while panels (e)–(g) are those for the descending track.

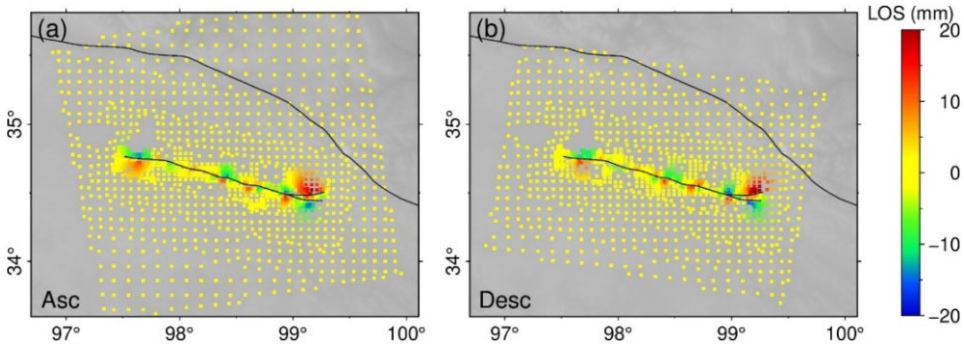

Figure 12. The predicted deformation by the poroelastic rebound mechanism. Panels (a) and (b) are those in the LOS directions of ascending and descending tracks, respectively.

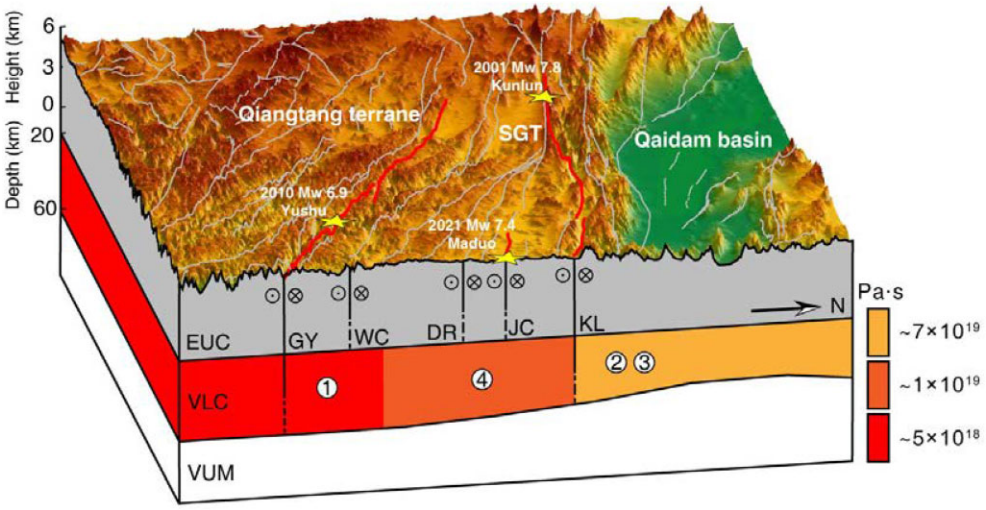

Figure 13. Schematic of lower crustal viscosity across the northeastern Tibet. Long red lines define the SGT region. GY, WC, DR, JC, KL denote the Ganzi-Yushu, Wudaoliang-Changshagongma, Dari, Jiangcuo and eastern Kunlun fault, respectively. EUC: elastic upper crust; VLC: viscoelastic lower crust; and VUM: viscoelastic upper mantle. Colours in VLC are corresponding to viscosities inferred from previous geodetic studies and ours: ① = Chen *et al.* (2022); ② = Liu *et al.* (2019); ③ = Zhao *et al.* (2021a) and ④ = this study.

geodetic observations (Wang & Shen 2020; Yue *et al.* 2022). However, the underlying mechanism is poorly understood.

The continental crustal strength is jointly controlled by the frictional strength of the upper crust and the rheological strength of the lower crust (Yue *et al.* 2022). Geophysical observations, such as the seismicity and coseismic ruptures extent, indicate similar seismogenic depths and similar upper crustal strength of the SGT (Yue *et al.* 2022), thus the whole strength of the crust may be governed by the underlying lower crustal layer. The obtained low viscosity beneath the SGT suggests a weak lower crust in contrast to that of the Qaidam basin and Qilian Mountains to the north, which may lead to distributed shear deformation within the terrane and negligible deformation in the north regions, respectively. Furthermore, both theoretical analysis and numerical simulations suggest that a weak lower crust tends to widen the deformation zone from the boundary fault in geologic time scales, which is accompanied by development of subparallel secondary faults (Roy & Royden 2000a,b). These theoretical results, as well as the weak strength of the lower crust, explain the distributed shear deformation and the growth of secondary faults with the SGT. Our results highlight that the rheology of the lower crust plays an important role on the tectonic deformation, fault evolution and associated seismic hazards.

5.4 Implications for shallow afterslip, frictional behaviour and coseismic shallow slip deficit

Afterslip that occurs under the coseismic stress perturbations, can elucidate the fault frictional characteristics (Marone *et al.* 1991). As demonstrated in previous studies (e.g. Zhou *et al.* 2018; Liu & Xu 2019), afterslip evolves following the rate-and-state frictional law:

$$U(t) = \frac{(a-b)\bar{\sigma}}{k} \ln\left(1 + \frac{Vkt}{(a-b)\bar{\sigma}}\right), \quad (7)$$

where U is the afterslip magnitude that varies with time since the earthquake (t); k, $\bar{\sigma}$ and V are the crustal stiffness, the effective normal stress and the initial slip rate after the earthquake, respectively. $(a-b)$ is the integrated fault frictional parameter.

Based on eq. (7) and the obtained time-dependent afterslip model in Section 4.2, we estimate $(a-b)$ values on fault patches. As shown by Liu & Xu (2019), the constitutive law in eq. (7) can be simplified as $U(t) = A\ln(1+t/\tau)$, where A is the magnitude factor and τ is the decay time of afterslip. Thus, we can calculate $(a-b)$ values by using $a-b = Ak/\bar{\sigma}$, with the approach shown in Kato. (2002) to calculate the effective normal stress ($\bar{\sigma}$). The crustal stiffness can be obtained by $k = G/h$, where G is the shear modulus (30 GPa) and h is the thickness of rate-strengthening region. Due to the unlikelihood of the fault rupture far beyond the depth of

aftershock cloud, we adopt $h = 20$ km in this study to analyse the fault frictional behaviour.

The inferred values of $(a—b)$ are on the order of $10^{-4} \sim 10^{-3}$ (Fig. 6c), at the lower bound of the laboratory results (10^{-3}–$10^{-2;}$ Marone 1998), which is consistent with that shown in Zhao *et al.* (2023). Both the $(a—b)$ values inferred from the stress-driven afterslip (Jin *et al.* 2023; Zhao *et al.* 2023) and kinematic afterslip (this study) indicate a rate-strengthening frictional property in the uppermost patches of the upper crust. Furthermore, the $(a—b)$ values on uppermost patches of the middle north-dipping segment (longitude 98.2–98.7°) are significantly higher than those in other fault regions, indicating a strong rate-strengthening frictional property. Combining with the low coseismic slip on these patches, we infer that uppermost fault patches may act as a barrier and have prevented the coseismic rupture from reaching the surface (Fig. 4c). Significant coseismic slip occurs on patches below the shallow rate-strengthening region, suggesting a variable slip behaviour (rate-weakening) on deep patches.

Whether the SSD in the middle fault segment (longitude 98.2–98.7°) has been filled by aseismic afterslip is important for future seismic hazard assessment. By comparing the coseismic slip along the strike of the fault, we observe an average slip deficit of ∼0.6 m in the middle segment, however, the inferred average afterslip is only ∼0.06 m there, which only compensates for a small part of the observed SSD (∼10 per cent). Previous studies suggested the maturity of the Jiangcuo fault is relatively low (e.g. Zhao *et al.* 2021b; Li *et al.* 2023), and dynamic simulations of earthquake cycles indicated abundant slow slip and creep in an immature fault (Thakur & Huang 2021). We therefore speculate that the middle segment might not be completely locked in interseismic periods, and/or partial accumulated strain had been released through slow slip/creep. In such a situation, the observed coseismic SSD is induced by the inhomogeneous strain accumulation along the fault. Fault creep on immature faults has been observed on continental strike-slip fault, such as the Northern San Andreas fault (e.g. Tong *et al.* 2013; Murray *et al.* 2014). However, due to the low slip rate (1–2 mm yr^{-1}) of the Jiangcuo fault (Zhu *et al.* 2021), monitoring its interseismic creep with geodetic observations remains challenging. Therefore, we cannot exclude other possibilities, such as the stress remaining unreleased or off-fault deformation occurred within the damage zone ameliorating the SSD (Dolan & Haravitch 2014).

6 CONCLUSIONS

In this paper, we study the co- and post-seismic deformation of the 2021 M_w 7.4 Maduo earthquake based on satellite image data. With coseismic InSAR and sPOT data, we first investigate the coseismic slip model of the Maduo earthquake. Inferred results reveal an asymmetric bilateral rupture pattern. Most coseismic slip is distributed at 3–15 km depth, leading to clear shallow slip deficit. Then, we investigate the mechanisms of the post-seismic deformation in the first 450 d following the 2021 M_w 7.4 Maduo earthquake. Combined GPS and InSAR observations reveal post-seismic deformation in both near- and far-field areas, suggesting that variable mechanisms are involved. Modelling results indicate that the observed post-seismic deformation is governed by a combined mechanism of afterslip and viscoelastic relaxation. Neglecting the viscoelastic relaxation effect will result in widespread afterslip on deep patches in the ductile layer. The inferred lower crustal viscosity at interior of the SGT suggests a low crustal strength, which may be responsible for the distributed shear deformation and development of secondary faults within the terrane. Besides, the frictional behaviour of the Jiangcuo fault revealed by afterslip suggests a rate-strengthening character on uppermost patches of the middle fault segment (longitude 98.2–98.7°), which may relate to the arrest of the coseismic slip and the significant coseismic slip deficit.

SUPPORTING INFORMATION

Supplementary data are available at *GJI* online.

Figure S1. The small baseline network of interferograms for ascending and descending tracks of Sentinel-1 data. Each circle represents one Sentinel-1 image acquisition and the red circles correspond to the reference image in the network. Perpendicular baseline values are with respect to the reference image. Each line represents an interferogram. The lines are colour-coded with average spatial coherence of corresponding interferogram.

Figure S2. Post-seismic InSAR displacement time-series and signal decomposition on selected pixels (P1–P4). Panels (a) and (f) show accumulated displacements in LOS directions of ascending and descending tracks and location of selected pixels. The black and red triangles are the original InSAR data and fitted result using eq. (1), respectively. The blue and green triangles show post-seismic displacement deformation caused by the Maduo earthquake and seasonal deformation caused by the permafrost effect. The location of pixels is shown in (a) and (f).

Figure S3. The observed and fitted GPS displacement time-series in this study. The black dots with red error bar and blue line represent the observed and fitted data after removing the background tectonic deformation and seasonal deformation, respectively.

Figure S4. Upper panels show grid-search results for dip angles of four fault segments based on observations. Lower panels draw grid-search results of four fault segments based on synthetic data. Based on these tests, we find that the input dip angles can be recovered reasonably well.

Figure S5. Checkerboard tests showing the resolving power of the observation. Panels (a) and (b) are input models with asperity of 24 km × 12 km and 12 km × 12 km, respectively. Panels (c) and (d) are corresponding recovered models.

Figure S6. The observed and predicted GPS displacement time-series by post-seismic model in this study. The red, blue and green lines represent the predictions by the afterslip + viscoelastic relaxation model, afterslip model and viscoelastic relaxation model, respectively. The black dots with grey error bar and black line represent the observed and fitted displacement time-series, respectively.

Table S1. Summary of the Sentinel-1 SAR data used to measure the coseismic deformation of the M_w 7.4 Maduo earthquake.

Table S2. Summary of the Sentinel-1 SAR data used to measure the post-seismic deformation of the M_w 7.4 Maduo earthquake.

Please note: Oxford University Press is not responsible for the content or functionality of any supporting materials supplied by the authors. Any queries (other than missing material) should be directed to the corresponding author for the paper.

ACKNOWLEDGMENTS

This work was supported by the National Key Research and Development Program of China (Grant No. 2022YFF0800703, 2023YFC3007302). We thank Yanqiang Wu and Yan Hu for support in GPS data collection. We thank Thomas R. Walter and Mahdi Motagh for their assistance in the InSAR data processing. We also thank the Editor Ana Ferreira and Reviewer Jihong Liu and one

anonymous reviewer for their valuable comments. The figures were drawn using the Generic Mapping Tools (GMT) software (Wessel & Smith 1998).

DATA AVAILABILITY

The InSAR data used in this study are publicly available and can be downloaded from (https://vertex.daac.asf.alaska.edu/)

AUTHOR CONTRIBUTION

Fei Chen (investigation, validation, writing—original draft), Faqi Diao (methodology, supervision, writing—review and editing), Mahmud Haghshenas Haghighi (data curation, writing—review & editing), Yuebing Wang (data curation, writing—review and editing), Yage Zhu (writing—review and editing), Rongjiang Wang (writing—review and editing) and Xiong Xiong (writing—review and editing).

CONFLICTS OF INTEREST

The authors declare that they have no competing interests.

REFERENCES

Baran, I., Stewart, M.P., Kampes, B.M., Perski, Z. & Lilly, P., 2003. A modification to the Goldstein radar interferogram filter. *IEEE Trans. Geosci. Remote Sens.,* **41**(9), 2114–2118.

Berardino, P., Fornaro, G., Lanari, R. & Sansosti, E., 2002. A new algorithm for surface deformation monitoring based on small baseline differential SAR interferograms. *IEEE Trans. Geosci. Remote Sens.,* **40**(11), 2375–2383.

Bürgmann, R. & Dresen, G., 2008. Rheology of the lower crust and upper mantle: evidence from rock mechanics, geodesy, and field observations. *Annu. Rev. Earth planet. Sci.,* **36,** 531–567.

Chen, C.W. & Zebker, H.A., 2001. Two-dimensional phase unwrapping with use of statistical models for cost functions in nonlinear optimization. *J. Opt. Soc. Am., A,* **18**(2), 338–351.

Chen, J. *et al.*, 2022. Magnitudes and patterns of large-scale permafrost ground deformation revealed by Sentinel-1 InSAR on the central Qinghai-Tibet Plateau. *Remote Sens. Environ.,* **268,** 112778. doi: 10.1016/j.rse.2021.112778.

Chen, Y., Hu, Y., Qian, L. & Meng, G., 2022. Early post-seismic deformation of the 2010 Mw 6.9 Yushu earthquake and its implication for lithospheric rheological properties. *Geophys. Res. Lett.,* **49**(15), doi:10.1029/2022GL098942.

Clark, M.K. & Royden, L.H., 2000. Topographic ooze: building the eastern margin of Tibet by lower crustal flow. *Geology,* **28**(8), 703–706.

Diao, F., Wang, R., Wang, Y., Xiong, X. & Walter, T.R., 2018. Fault behavior and lower crustal rheology inferred from the first seven years of postseismic GPS data after the 2008 Wenchuan earthquake. *Earth planet. Sci. Lett.,* **495,** 202–212.

Diao, F., Wang, R., Xiong, X. & Liu, C., 2021. Overlapped post-seismic deformation caused by afterslip and viscoelastic relaxation following the 2015 Mw 7.8 Gorkha (Nepal) earthquake. *J. geophys. Res.,* **126**(3), doi:10.1029/2020JB020378.

Diao, F., Xiong, X., Wang, R., Walter, T.R., Wang, Y. & Wang, K., 2019. Slip rate variation along the Kunlun fault (Tibet): results from new GPS observations and a viscoelastic earthquake-cycle deformation model. *Geophys. Res. Lett.,* **46**(5), 2524–2533.

Dolan, J.F. & Haravitch, B.D., 2014. How well do surface slip measurements track slip at depth in large strike-slip earthquakes? The importance of fault structural maturity in controlling on-fault slip versus off-fault surface deformation. *Earth planet. Sci. Lett.,* **388,** 38–47.

Fang, J. *et al.*, 2022. Earthquake cycle deformation associated with the 2021 Mw 7.4 Maduo (Eastern Tibet) Earthquake: an intrablock rupture event on a slow-slipping fault from Sentinel-1 InSAR and teleseismic data. *J. geophys. Res.,* **127**(11), e2022JB024268.

Farr, T.G. & Kobrick, M., 2000. Shuttle radar topography mission produces a wealth of data. *EOS, Trans. Am. geophys. Un.,* **81**(48), 583–585.

Fattahi, H. & Amelung, F., 2013. DEM error correction in InSAR time-series. *IEEE Trans. Geosci. Remote Sens.,* **51**(7), 4249–4259.

Feng, W., Samsonov, S., Qiu, Q., Wang, Y., Zhang, P., Li, T. & Zheng, W., 2020. Orthogonal fault rupture and rapid post-seismic deformation following 2019 Ridgecrest, California, earthquake sequence revealed from geodetic observations. *Geophys. Res. Lett.,* **47**(5), e2019GL086888.

Freed, A.M., Hashima, A., Becker, T.W., Okaya, D.A., Sato, H. & Hatanaka, Y., 2017. Resolving depth-dependent subduction zone viscosity and afterslip from post-seismic displacements following the 2011 Tohoku-oki, Japan earthquake. *Earth planet. Sci. Lett.,* **459,** 279–290.

Fukuda, J. & Johnson, K.M., 2021. Bayesian inversion for a stress-driven model of afterslip and viscoelastic relaxation: method and application to post-seismic deformation following the 2011 Mw 9.0 Tohoku-Oki earthquake. *J. geophys. Res.,* **126**(5), doi:10.1029/2020JB021620.

Gan, W., Zhang, P., Shen, Z.K., Niu, Z., Wang, M., Wan, Y., Zhou, D. & Cheng, J., 2007. Present-day crustal motion within the Tibetan Plateau inferred from GPS measurements. *J. geophys. Res.,* **112**(B8), doi:10.1029/2005JB004120.

He, K., Wen, Y., Xu, C. & Zhao, Y., 2021a. Fault geometry and slip distribution of the 2021 Mw 7.4 Maduo, China, earthquake inferred from InSAR measurements and relocated aftershocks. *Seismol. Res. Lett.,* **93**(1), 8–20.

He, L. *et al.*, 2021b. Coseismic and early post-seismic slip models of the 2021 Mw 7.4 Maduo earthquake (western China) estimated by space-based geodetic data. *Geophys. Res. Lett.,* **48**(24), doi:10.1029/2021GL095860.

Herring, T.A., King, R.W. & McClusky, S.C., 2010a. *GAMIT Reference Manual, GPS Analysis at MIT, Release 10.4*. Massachusetts Institute of Technology.

Herring, T.A., King, R.W. & McClusky, S.C., 2010b. *GLOBK Reference Manual, Global Kalman Filter VLBI and GPS Analysis Program, Release 10.4,* Massachusetts Institute of Technology.

Hong, S. & Liu, M., 2021. Post-seismic deformation and afterslip evolution of the 2015 Gorkha earthquake constrained by InSAR and GPS observations. *J. geophys. Res.,* **126**(7), doi:10.1029/2020JB020230.

Hu, Y., Burgmann, R., Banerjee, P., Feng, L., Hill, E.M., Ito, T., Tabei, T. & Wang, K., 2016. Asthenosphere rheology inferred from observations of the 2012 Indian Ocean earthquake. *Nature,* **538**(7625), 368–372.

Jiang, C., Yang, Y. & Zheng, Y., 2014. Penetration of mid-crustal low velocity zone across the Kunlun fault in the NE Tibetan Plateau revealed by ambient noise tomography. *Earth planet. Sci. Lett.,* **406,** 81–92.

Jin, Z. & Fialko, Y., 2021. Coseismic and early post-seismic deformation due to the 2021 M7. 4 Maduo (China) earthquake. *Geophys. Res. Lett.,* **48**(21), e2021GL095213.

Jin, Z., Fialko, Y., Yang, H. & Li, Y., 2023. Transient deformation excited by the 2021 M7.4 Maduo (China) earthquake: evidence of a deep shear zone. *J. geophys. Res.,* **128,** e2023JB026643.

Jolivet, R., Grandin, R., Lasserre, C., Doin, M.P. & Peltzer, G., 2011. Systematic InSAR tropospheric phase delay corrections from global meteorological reanalysis data. *Geophys. Res. Lett.,* **38**(17), doi:10.1029/2011GL048757.

Jónsson, S., Segall, P., Pedersen, R. & Björnsson, G., 2003. Post-earthquake ground movements correlated to pore-pressure transients. *Nature,* **424**(6945), 179–183.

Kato, N., 2002. Seismic cycle on a strike-slip fault with rate-and state-dependent strength in an elastic layer overlying a viscoelastic half-space. *Earth, Planets Space,* **54**(11), 1077–1083.

Li, C., Li, T., Shan, X. & Zhang, G., 2023. Extremely large off-fault deformation during the 2021 Mw 7.4 Maduo, Tibetan Plateau, earthquake. *Seismol. Res. Lett.,* **94**(1), 39–51.

Li, Q., Wan, Y., Li, C., Tang, H., Tan, K. & Wang, D., 2022. Source process featuring asymmetric rupture velocities of the 2021 Mw 7.4 Maduo, China, earthquake from teleseismic and geodetic data. *Seismol. Res. Lett.,* **93**(3), 1429–1439.

Liu, C., Lay, T., Brodsky, E.E., Dascher-Cousineau, K. & Xiong, X., 2019. Coseismic rupture process of the large 2019 ridgecrest earthquakes from joint inversion of geodetic and seismological observations. *Geophys. Res. Lett.,* **46**(21), 11 820–11 829.

Liu, S., Xu, X., Klinger, Y., Nocquet, J.M., Chen, G., Yu, G. & Jónsson, S., 2019. Lower crustal heterogeneity beneath the northern Tibetan Plateau constrained by GPS measurements following the 2001 Mw7.8 Kokoxili earthquake. *J. geophys. Res.,* **124**(11), 11 992–12 022.

Liu, X. & Xu, W., 2019. Logarithmic model joint inversion method for coseismic and post-seismic slip: application to the 2017 Mw 7.3 Sarpol Zahāb earthquake, Iran. *J. geophys. Res.,* **124**(11), 12 034–12 052.

Marone, C., 1998. Laboratory-derived friction laws and their application to seismic faulting. *Annu. Rev. Earth planet. Sci.,* **26**(1), 643–696.

Marone, C.J., Scholtz, C.H. & Bilham, R., 1991. On the mechanics of earthquake afterslip. *J. geophys. Res.,* **96**(B5), 8441–8452.

Michel, R., Avouac, J.P. & Taboury, J., 1999. Measuring ground displacements from SAR amplitude images: application to the landers earthquake. *Geophys. Res. Lett.,* **26,** 875–878.

Muñoz-Sabater, J., 2019. ERA5-Land hourly data from 1981 to present. *Copernicus Climate Change Service (C3S) Climate Data Store (CDS)*. (Accessed on 08-04-2022).

Murray, J.R., Minson, S.E. & Svarc, J.L., 2014. Slip rates and spatially variable creep on faults of the northern San Andreas system inferred through bayesian inversion of Global Positioning System data. *J. geophys. Res.,* **119**(7), 6023–6047.

Nikolaidis, R., 2002. Observation of geodetic and seismic deformation with the global positioning system, *PhD thesis*. University of California, San Diego.

Pan, J. *et al.*, 2022. Co-seismic rupture of the 2021, Mw 7.4 Maduo earthquake (northern Tibet): short-cutting of the Kunlun fault big bend. *Earth planet. Sci. Lett.,* **594,** doi:10.1016/j.epsl.2022.117703.

Qiao, X., Zhou, Y. & Zhang, P., 2022. Along-strike variation in fault structural maturity and seismic moment deficits on the Yushu-Ganzi-Xianshuihe fault system revealed by strain accumulation and regional seismicity. *Earth planet. Sci. Lett.,* **596,** doi:10.1016/j.epsl.2022.117799.

Roy, M. & Royden, L.H., 2000a. Crustal rheology and faulting at strike-slip plate boundaries: 1. An analytic model. *J. geophys. Res.,* **105**(B3), 5583–5597.

Roy, M. & Royden, L.H., 2000b. Crustal rheology and faulting at strike-slip plate boundaries: 2. Effects of lower crustal flow. *J. geophys. Res.,* **105**(B3), 5599–5613.

Royden, L.H., Burchfiel, B.C. & van der Hilst, R.D., 2008. The geological evolution of the Tibetan Plateau. *Science,* **321**(5892), 1054–1058.

Simons, M., Fialko, Y. & Rivera, L., 2002. Coseismic deformation from the 1999 Mw 7.1 Hector Mine, California, earthquake as inferred from InSAR and GPS observations. *Bull. seism. Soc. Am.,* **92**(4), 1390–1402.

Sun, T. *et al.*, 2014. Prevalence of viscoelastic relaxation after the 2011 Tohoku-oki earthquake. *Nature,* **514**(7520), 84–87.

Tapponnier, P., Xu, Z., Roger, F., Meyer, B., Arnaud, N., Wittlinger, G. & Jingsui, Y., 2001. Oblique stepwise rise and growth of the Tibet Plateau. *Science,* **294,** 1671–1677.

Thakur, P. & Huang, Y., 2021. Influence of fault zone maturity on fully dynamic earthquake cycles. *Geophys. Res. Lett.,* **48**(17), e2021GL094679.

Tian, Z., Freymueller, J.T. & Yang, Z., 2020. Spatio-temporal variations of afterslip and viscoelastic relaxation following the Mw 7.8 Gorkha (Nepal) earthquake. *Earth planet. Sci. Lett.,* **532,** doi:10.1016/j.epsl.2019.116031.

Tong, X., Sandwell, D.T. & Smith-Konter, B., 2013. High-resolution interseismic velocity data along the San Andreas Fault from GPS and InSAR. *J. geophys. Res.,* **118**(1), 369–389.

Wang, K., Hu, Y. & He, J., 2012. Deformation cycles of subduction earthquakes in a viscoelastic Earth. *Nature,* **484**(7394), 327–332.

Wang, M. & Shen, Z.K., 2020. Present-day crustal deformation of continental China derived from GPS and its tectonic implications. *J. geophys. Res.,* **125**(2), doi:10.1029/2019JB018774.

Wang, M., Wang, F., Jiang, X., Tian, J., Li, Y., Sun, J. & Shen, Z.-K., 2022. GPS determined coseismic slip of the 2021 Mw7.4 Maduo, China, earthquake and its tectonic implication. *Geophys. J. Int.,* **228**(3), 2048–2055.

Wang, R., Diao, F. & Hoechner, A., 2013. SDM—a geodetic inversion code incorporating with layered crust structure and curved fault geometry, in *EGU General Assembly Conference Abstracts,* EGU2013-2411.

Wang, R., Lorenzo-Martín, F. & Roth, F., 2006. PSGRN/PSCMP—a new code for calculating co-and post-seismic deformation, geoid and gravity changes based on the viscoelastic-gravitational dislocation theory. *Comput. Geosci.,* **32**(4), 527–541.

Wang, W., Fang, L., Wu, J., Tu, H., Chen, L., Lai, G. & Zhang, L., 2021. Aftershock sequence relocation of the 2021 Ms7.4 Maduo earthquake, Qinghai, China. *Sci. China D,* **64**(8), 1371–1380.

Wegnüller, U., Werner, C., Strozzi, T., Wiesmann, A., Frey, O. & Santoro, M., 2016. Sentinel-1 support in the GAMMA software. *Proc. Comput. Sci.,* **100,** 1305–1312.

Wessel, P. & Smith, W.H., 1998. New, improved version of Generic Mapping Tools released. *EOS, Trans. Am. geophys. Un.,* **79**(47), 579–579.

Xiong, W. *et al.*, 2022. Coseismic slip and early afterslip of the 2021 Mw 7.4 Maduo, China earthquake constrained by GPS and InSAR data. *Tectonophysics,* **840,** doi:10.1016/j.tecto.2022.229558.

Xiong, X., Shan, B., Zheng, Y. & Wang, R., 2010. Stress transfer and its implication for earthquake hazard on the Kunlun fault, Tibet. *Tectonophysics,* **482**(1-4), 216–225.

Yuan, Z., Li, T., Su, P., Sun, H., Ha, G., Guo, P., Chen, G. & Jobe, J.T., 2022. Large surface-rupture gaps and low surface fault slip of the 2021 Mw 7.4 Maduo earthquake along a low-activity strike-slip fault, Tibetan Plateau. *Geophys. Res. Lett.,* **49**(6), doi:10.1029/2021GL096874.

Yue, H. *et al.*, 2022. Rupture process of the 2021 M7.4 Maduo earthquake and implication for deformation mode of the Songpan-Ganzi terrane in Tibetan Plateau. *Proc. Natl. Acad. Sci.,* **119**(23), e2116445119.

Zhan, Y. *et al.*, 2021. Deep structure and seismogenic pattern of the 2021.5.22 Madoi (Qinghai) Ms 7.4 earthquake. *Chin. J. Geophys.,* **64**(7), 2232–2252 (in Chinese with English abstract).

Zhang, Y., Fattahi, H. & Amelung, F., 2019. Small baseline InSAR time series analysis: unwrapping error correction and noise reduction. *Comput. Geosci.,* **133,** doi:10.31223/osf.io/9sz6m.

Zhang, Y., Feng, W., Li, X., Liu, Y., Ning, J. & Huang, Q., 2021. Joint inversion of rupture across a fault stepover during the 8 August 2017 Mw 6.5 Jiuzhaigou, China, earthquake. *Seismol. Res. Lett.,* **92**(6), 3386–3397.

Zhao, D., Qu, C., Bürgmann, R., Gong, W. & Shan, X., 2021a. Relaxation of Tibetan lower crust and afterslip driven by the 2001 Mw7.8 Kokoxili, China, earthquake constrained by a decade of geodetic measurements. *J. geophys. Res.,* **126**(4), doi:10.1029/2020JB021314.

Zhao, D., Qu, C., Chen, H., Shan, X., Song, X. & Gong, W., 2021b. Tectonic and geometric control on fault kinematics of the 2021 Mw7.3 Maduo (China) earthquake inferred from interseismic, coseismic, and post-seismic InSAR observations. *Geophys. Res. Lett.,* **48**(18), e2021GL095417.

Zhao, L., Xu, W., Xie, L., Zhao, D., Zhu, Z., Wu, P. & Guo, H., 2023. Fault geometry and low frictional control of the near-field post-seismic deformation of the 2021 Mw 7.3 Maduo earthquake. *Tectonophysics,* **863,** doi:10.1016/j.tecto.2023.230000.

Zhou, Y., Thomas, M.Y., Parsons, B. & Walker, R.T., 2018. Time-dependent post-seismic slip following the 1978 M 7.3 Tabas-e-Golshan, Iran earthquake revealed by over 20 years of ESA InSAR observations. *Earth planet. Sci. Lett.,* **483,** 64–75.

Zhu, Y., Diao, F., Fu, Y., Liu, C. & Xiong, X., 2021. Slip rate of the seismogenic fault of the 2021 Maduo earthquake in western China inferred from GPS observations. *Sci. China D,* **64,** 1363–1370.